

# The One-dimensional Fourier Representation and Large Angular Scale Foreground Contamination in the 3-year Wilkinson Microwave Anisotropy Probe data

Lung-Yih Chiang<sup>1</sup>, Peter Coles<sup>2,3</sup>, Pavel D Naselsky<sup>1</sup>, Poul Olesen<sup>1</sup>

<sup>1</sup> Niels Bohr Institute, Blegdamsvej 17, DK-2100 Copenhagen, Denmark

<sup>2</sup> School of Physics & Astronomy, University of Nottingham, University Park, Nottingham NG7 2RD, United Kingdom

<sup>3</sup> Niels Bohr Institute, Niels Bohr International Academy, Blegdamsvej 17, DK-2100 Copenhagen, Denmark

E-mail: [chiang@nbi.dk](mailto:chiang@nbi.dk), [peter.coles@nottingham.ac.uk](mailto:peter.coles@nottingham.ac.uk), [naselsky@nbi.dk](mailto:naselsky@nbi.dk), [polesen@nbi.dk](mailto:polesen@nbi.dk)

**Abstract.** We employ the one-dimensional Fourier representation (1DFR) to analyze the 3-year *WMAP* de-biased internal linear combination (DILC) map and its possible contamination by galactic foregrounds. The 1DFR is a representation of the spherical harmonic coefficients for each  $\ell$ -mode using an inverse Fourier transform into one-dimensional curves. Based on the *a priori* assumption that the CMB signal should be statistically independent of, and consequently have no significant correlation with, any foregrounds, we cross-correlate the 1DFR curves of  $2 \leq \ell \leq 10$  modes, which are claimed by the *WMAP* team to be free of contamination and suitable for whole sky analysis. We find that 8 out of the 9 modes are negatively cross correlated with the foreground maps, an event which has a probability of only  $9/512 \simeq 0.0176$  for uncorrelated signals. Furthermore, the local extrema of the 1DFR curves between the DILC and those of the foregrounds for  $\ell = 2$  and 6 are correlated with significance level below 0.04. We also discuss the minimum variance optimization method and use the properties of the measured cross-correlation to estimate the possible level of contamination present in the DILC map.

PACS numbers: 98.80.-k, 95.85.Bh, 98.70.Vc, 95.75.-z

*Keywords:* cosmology: cosmic microwave background — cosmology: observations — methods: data analysis

## 1. Introduction

The cosmic microwave background (CMB) radiation contains a wealth of information about our Universe. Not only does the angular power spectrum of the CMB temperature fluctuations allow us to determine cosmological parameters that shape our understanding of the Universe, but the issue of primordial Gaussianity and statistical isotropy of the CMB also taps the most fundamental principle in cosmology, and any robust detection of a deviation would have far-reaching and indeed revolutionary implications.

Interpreting the term “Gaussianity” in the most relevant way for cosmology, i.e. as meaning that the fluctuations form a statistically homogeneous and isotropic Gaussian random field [3, 7], the issue of non-Gaussianity in the CMB data was first raised by [29] in the COBE data [56]. After the release of the 1-year Wilkinson Microwave Anisotropy Probe (*WMAP*) data [4, 5, 41, 37], departures from Gaussianity have been detected with various methods [12, 32, 14, 53, 28, 62, 9, 35, 47, 43, 49, 45, 61, 22]. Although Gaussianity (as we define it) requires statistical isotropy, a special focus and results on the breaking of large-scale statistical isotropy have been reported in [60, 19, 27, 15, 55, 42, 6, 1]. Among them, the most notable anomaly involves the alignment of the quadrupole and octupole alignment in the general direction of Virgo. In the 3-year *WMAP* data [38, 57] the previously detected departures from Gaussianity and statistical isotropy still persist [11, 17, 46, 16]. The question is whether they are attributed to foreground residuals [2], systematic errors [8], local structures [39] or even new physics [40, 33].

However, it is important to eliminate the least exciting possibilities before getting carried away by the most exotic ones. In particular, one has to be cautious about foreground residuals as they are surely present in the derived CMB map. The elimination of foregrounds and the extraction of CMB signal is based on the concept of minimum variance optimization with the *a priori* assumption that CMB and the foregrounds are statistically independent: linearly combining all available maps and minimizing the variance of the combined map to reduce the foreground residuals as much as possible. The 3-year de-biased internal linear combination (DILC) map is based on such a concept by the *WMAP* science team. This approach can certainly help to achieve the optimal estimate of the angular power spectrum for the CMB. It cannot, however, guarantee the optimal morphology (spatial distribution). Since most of the anomalies, with the exception of the reported low quadrupole power [24, 19, 25], are related to the pattern of fluctuations rather than simply their amplitude, one needs to check the derived CMB map very carefully before any scientific conclusion is reached. In this light, several authors have investigated possible foreground contaminations [48, 20, 21, 52] and the effect of different subtraction methods [18, 54].

The *a priori* assumption that the CMB and the foregrounds are statistically independent and thus have no significant cross-correlation is not only the backbone of the minimum variance optimization method, it is also the most basic principle (preceding Gaussianity of the CMB), furnishing the most fundamental statistical test for foreground

cleaning. Note that statistical independence involves an ensemble of universes, there will, therefore, inevitably be accidental cross-correlations caused by chance alignments, particularly on large angular scales due to the cosmic variance effect [63].

Efforts on the investigation on large-scale foreground contamination by direct cross-correlation were made in the harmonic domain. Based on the close connection between the phases of the spherical harmonic modes, and morphology [10], [50, 51, 13] examine foreground residuals by cross-correlation of phases between the *WMAP* internal linear combination maps and the derived foreground maps.

In this paper, we use a new representation of the spherical harmonic modes to analyze the cross correlation between the DILC and foreground maps. Instead of using the the two-dimensional spheres, we use an inverse Fourier transform on the spherical harmonic modes for each  $\ell$  producing one-dimensional curves for each harmonic scale. We therefore call such representation one-dimensional Fourier representation (1DFR). Chiang and Naselsky [13] first devised the 1DFR to illustrate connection between phase coupling and morphology, particularly relating to local extrema higher than  $3\sigma$ . Chiang, Naselsky and Coles [11] use the same representation to demonstrate the anomalies in the distribution of global extrema of the 1DFR curves of the DILC map for the  $\ell \leq 10$  modes.

This paper is arranged as follows. In Section 2 we summarize the Gaussian random hypothesis of the CMB. In Section 3 we introduce the 1DFR and its properties and advantages. We then use simple cross-correlation and extremum correlation to examine foreground contamination in the DILC map in Section 4. We discuss the minimum variance optimization method and use cross-correlation coefficients to estimate the level of foreground contamination in Section 5. The conclusions are presented in Section 6.

## 2. Gaussian Random hypothesis of the CMB

The statistical characterization of CMB temperature fluctuations (against the CMB isotropic temperature  $T_0 = 2.725$  K) on a sphere can be expressed as a sum over spherical harmonics:

$$T(\theta, \varphi) = \sum_{\ell=0}^{\infty} \sum_{m=-\ell}^{\ell} a_{\ell m} Y_{\ell m}(\theta, \varphi), \quad (2.1)$$

where the  $Y_{\ell m}(\theta, \varphi)$  are spherical harmonic functions, defined in terms of the Legendre polynomials  $P_{\ell m}$  using

$$Y_{\ell m}(\theta, \varphi) = (-1)^m \sqrt{\frac{(2\ell+1)(\ell-m)!}{4\pi(\ell+m)!}} P_{\ell m}(\cos \theta) \exp(im\varphi), \quad (2.2)$$

and the  $a_{\ell m}$  are complex coefficients which can be expressed with  $a_{\ell m} = |a_{\ell m}| \exp(i\Phi_{\ell m})$  and  $\Phi_{\ell m}$  are the phases. We use the Condon-Shortly definition for the spherical harmonic decomposition. Isotropic Gaussian random CMB temperature fluctuations on a sphere, of the type that result from the simplest versions of the inflation paradigm, possess spherical harmonic coefficients  $a_{\ell m}$  whose real and imaginary parts are mutually

independent and both Gaussian, or equivalently, the amplitudes  $|a_{\ell m}|$  are Rayleigh distributed with random phases [3, 7]. The statistical properties are then completely specified by the second-order statistics, the angular power spectrum  $C_\ell$ ,

$$\langle a_{\ell m} a_{\ell' m'}^* \rangle = C_\ell \delta_{\ell\ell'} \delta_{mm'}. \quad (2.3)$$

Since  $T$  is always real, the complex vectors of the  $a_{\ell m}$  on the Argand plane for  $m < 0$  are mirror images of  $m > 0$  with respect to  $x$  axis for even  $m$ , and with respect to  $y$  axis for odd  $m$ . The statistics for real signal on a sphere are therefore registered only in the spherical harmonic coefficients  $a_{\ell m}$  for  $m \geq 0$ .

### 3. One dimensional Fourier representation of the spherical harmonic coefficients

Recent studies of the large angular scale properties for the CMB temperature anisotropy [60, 19, 55, 42] are based on the composite map constructed for each  $\ell$  by summing all the  $m$  modes pertaining to that  $\ell$ :

$$T_\ell(\theta, \varphi) = \sum_{m=-\ell}^{\ell} a_{\ell m} Y_{\ell m}(\theta, \varphi). \quad (3.1)$$

Alternatively, one can represent  $a_{\ell m}$  in each  $\ell$  by an inverse Fourier transform, as the  $a_{\ell m}$  is now a function of a single variable  $m$ . Such a 1DFR for  $a_{\ell m}$  from the spherical harmonic decomposition of the sky is written as

$$T_\ell(\varphi) = \sum_{m=-\ell}^{\ell} a_{\ell m} \exp(im\varphi) = a_{\ell 0} + 2 \sum_{m=1}^{\ell} |a_{\ell m}| \cos(m\varphi + \Phi_{\ell m}), \quad (3.2)$$

where for the negative  $m$  we use the complex conjugate ( $a_{\ell, -m} = a_{\ell m}^*$ ) to make  $T_\ell(\varphi)$  real. As we have mentioned for real  $T$  on a sphere the statistics are registered only in  $m \geq 0$  modes, the  $T_\ell(\varphi)$  curves assembled in this way contain the same amount of information as the spherical  $T_\ell(\theta, \varphi)$ . The variance for each curve is then

$$\sigma_\ell^2 = \frac{1}{2\pi} \int_0^{2\pi} [T_\ell(\varphi) - \overline{T}_\ell]^2 d\varphi = 2 \sum_{m=1}^{\ell} |a_{\ell m}|^2. \quad (3.3)$$

For a Gaussian Random Field (GRF), the  $|a_{\ell m}|$  have a Rayleigh distribution, so  $\sigma_\ell^2$  has a chi-square distribution.

#### 3.1. Comparison between 1DFR and integration on $\theta$ of the composite maps

Since the 1DFR results in  $\Delta T$  as a single function of  $\varphi$ , such representation is therefore similar to the integration on  $\theta$  used in the composite maps:

$$\int_0^\pi T_\ell(\theta, \varphi) d\theta. \quad (3.4)$$

There are, however, some subtleties. Equation (3.1) can be written as follows

$$T_\ell(\theta, \varphi) = \sqrt{\frac{2\ell+1}{4\pi}} \left\{ a_{\ell 0} P_{\ell 0}(\cos \theta) + 2 \sum_{m=1}^{\ell} \left[ (-1)^m \sqrt{\frac{(\ell-m)!}{(\ell+m)!}} |a_{\ell m}| \cos(m\varphi + \Phi_{\ell m}) P_{\ell m}(\cos \theta) \right] \right\}. \quad (3.5)$$

As  $\int P_{\ell m}(\cos \theta) d\theta = 0$  for odd  $\ell + m$ , the curves from the integration over  $\theta$  from the composite maps have contributions from only the odd  $m$  part for odd  $\ell$  and the even  $m$  part for even  $\ell$ . Therefore for odd  $\ell$ , the  $(-1)^m$  term inverts the resulting temperature  $T$  as seen from the 1DFR. (As we use the Condon-Shortley definition for the spherical harmonic functions,  $\int P_{\ell m}(\cos \theta) d\theta$  is always positive for  $m > 0$  and 0 for  $m = 0$ ). Accordingly, in Figure 1, for the odd  $\ell$  curves the amplitudes are multiplied by  $-1$  to facilitate direct comparison. The  $\varphi$  coordinate of the 1DFR is also plotted backwards in order to match the Galactic longitude coordinate  $l$  (not to be confused with the spherical harmonic mode  $\ell$ ; see Figure 2 (top panel)).

Moreover, the integration over  $\theta$  results in more symmetric curves than the simple 1DFR, where equal footing is given to each  $a_{\ell m}$  in the summation. As shown in Figure 1, the curves (red) obtained by integration of  $\theta$  from the composite maps show repetitions for  $\varphi$  at  $[0, 180^\circ]$  and  $[-180^\circ, 0]$ .

### 3.2. Characteristics of the 1DFR

The 1DFR assembles spherical harmonic coefficients into one-dimensional curves, so the information on  $\theta$  direction is lost, compared with standard two-dimensional spherical maps. Nevertheless, the morphology and statistics registered in the complex  $a_{\ell m}$  sequence should still manifest themselves in this representation. For a Gaussian random field on a sphere, the real and imaginary parts of the spherical harmonic coefficients  $a_{\ell m}$  in each  $\ell$  are mutually independent and both Gaussian distributed with zero mean and variance  $C_\ell/2$ , where  $C_\ell$  is its angular power spectrum. Thus if the  $a_{\ell m}$  are a result of Gaussian process, the 1DFR  $T_\ell(\varphi)$  curves shall possess all the usual Gaussian random properties such as two-point correlation, peak statistics, and Minkowski functionals... etc..

One of the 1DFR characteristics is that the  $a_{\ell 0}$  modes contribute to the 1D curves only a constant shift without altering the morphology, whereas in spherical harmonic composition it produces modulation in  $\theta$  direction,  $a_{\ell 0} P_{\ell 0}(\cos \theta)$ . This is useful when one is to compare two sets of  $a_{\ell m}$  with standard cross-correlation, particularly when one of them is from a foreground map. Standard analysis on large angular scale (low multipole) anomalies is performed on a composite map by Equation (3.1): a full-sky map synthesized from the  $a_{\ell m}$  from  $-m$  to  $m$  for each  $\ell$  (see Figure 2 top panel as an example). For foreground maps defined in Galactic coordinate system, the emission near the Galactic plane dominates the signal, which is then spherical-harmonic transformed into high amplitudes of  $a_{\ell 0}$  for even  $\ell$  (Figure 2 bottom), which produce a prominent belt in the composite maps, making them rather difficult to analyze under such situation.

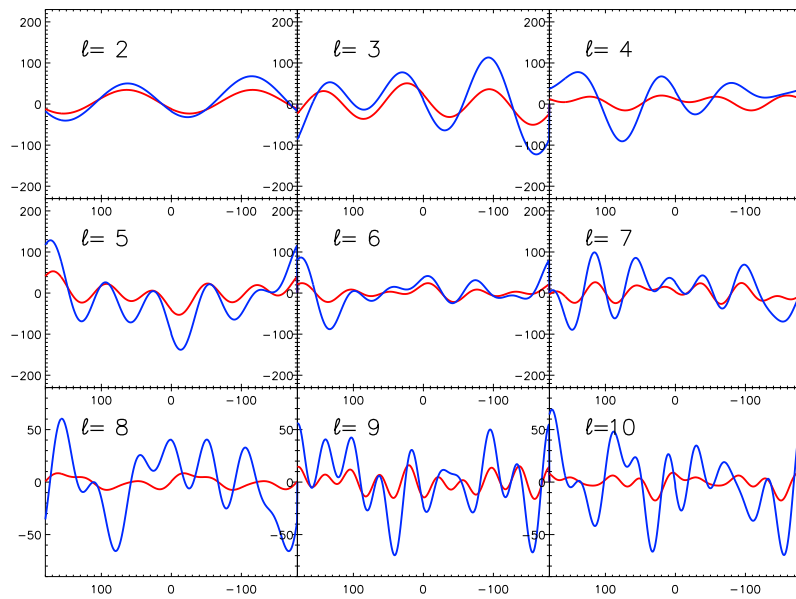


**Figure 1.** Comparison of the 1DFR of the DILC map (blue curves) and the  $T$  distribution curves from integration of  $T_\ell(\theta, \varphi)$  on  $\theta$  direction (red curves). The  $x$  axis is  $\varphi$  and is plotted reversely to follow the conventional Galactic longitude coordinate  $l$  and the  $y$  axis is in unit of thermodynamic temperature ( $\mu\text{K}$ ). Note that the amplitude of the 1DFR curves for odd  $\ell$  is multiplied by  $-1$  in order for comparison with those from integration on  $\theta$ .

#### 4. 1DFR and Foreground contamination in the DILC map

In this section we investigate foreground contamination in the WMAP 3-year DILC map. It is based on the *a priori* assumption that the CMB (at the background) should have no “knowledge” about what the foregrounds look like. So if the derived DILC map more or less reflects the morphology of true CMB, the DILC and foregrounds should have little or no resemblance to it; we can also see how clean is the derived DILC by directly comparing the morphology.

Firstly, in the top mosaic of Figure 3 we plot the 1DFR curves for the DILC (blue curves) and those of the WMAP derived foreground maps at Q (orange), V (green) and W (red) channels. The foreground maps are the sum of the synchrotron, free-free and dust templates obtained via Maximum Entropy Method [38]. As one can see, the most striking feature is the significant anti-correlation between the DILC and foregrounds for the quadrupole ( $\ell = 2$ ).

In the bottom mosaic of Figure 3 we plot, on a unit circle for each 1DFR curve, the positions of local extrema: all  $\varphi$  for  $dT_\ell/d\varphi = 0$  and  $d^2T_\ell/d\varphi^2 \neq 0$ . The angle between each sign and the positive  $x$  axis is  $\varphi$  for each local extremum position. The blue filled signs are from the DILC and the open signs the foreground map at Q (orange), V (green) and W (red) channels. We use circles and diamonds to denote peaks ( $d^2T_\ell/d\varphi^2 < 0$ ) and troughs ( $d^2T_\ell/d\varphi^2 > 0$ ), respectively. The size of the signs is  $\simeq 5^\circ$  so that one can see there are 12 out of totally 16 local extrema for  $\ell = 10$  DILC 1DFR curves with W channel foreground map 1DFR local extrema located within  $5^\circ$ .

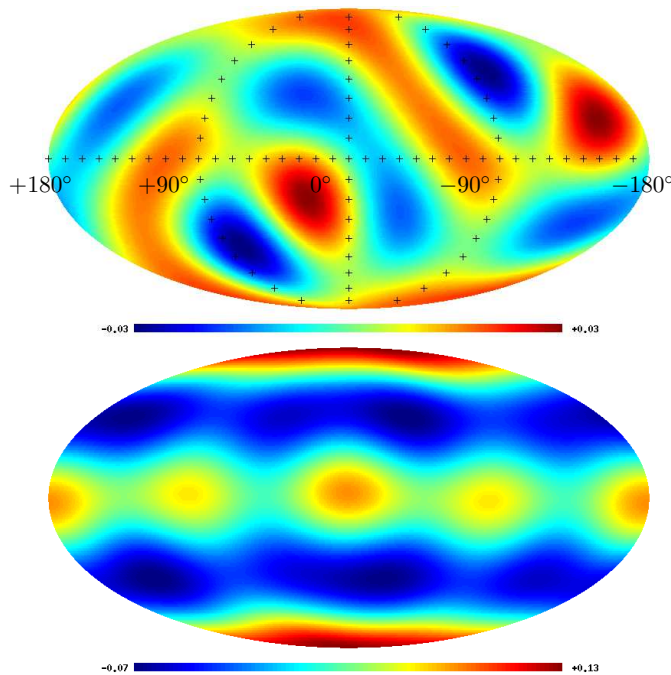


**Figure 2.** The composite map of  $\ell = 4$  from DILC map (top) and that of  $\ell = 4$  from the W channel foreground map (bottom). One can see the dominant stripes of the foreground composite map caused by  $a_{\ell 0} P_{\ell 0}(\cos \theta)$ , which makes it difficult to be compared with the DILC composite map.

In what follows, we employ cross correlation and correlation of extrema of the 1DFR curves to illustrate the foreground contamination in the DILC map. The cross correlation is a measure of “trend”: two curves will yield strong cross correlation if both go up or down in tandem at the same interval of  $\varphi$ . However, any correlation will be cancelled out if they match on one half of  $\varphi$ , but on the other they are opposite. Although cross and extremum correlation are not totally independent, it is therefore intuitively helpful to examine both properties.

#### 4.1. Cross correlations of the DILC map with the WMAP derived foreground maps

We use cross-correlation to quantify the foreground contamination in the DILC map:

$$X_{\ell}^{ij} = \frac{(2\pi)^{-1} \int_0^{2\pi} [T_{\ell}^i(\varphi) - \overline{T_{\ell}^i}] [T_{\ell}^j(\varphi) - \overline{T_{\ell}^j}] d\varphi}{\sigma_{\ell}^i \sigma_{\ell}^j}, \quad (4.1)$$

where  $T_{\ell}^i(\varphi)$  indicates the 1DFR curve of multipole number  $\ell$  at  $\varphi$  of  $i$  map,  $\sigma_{\ell}^i$  is the standard deviation of the curve. The  $X$  coefficients range from  $-1$  to  $1$ . In Figure 4 we show the  $X$  coefficients between 1DFR curves of the DILC and those of the foregrounds. First of all, if the DILC map is uncorrelated with the foregrounds, the probabilities for

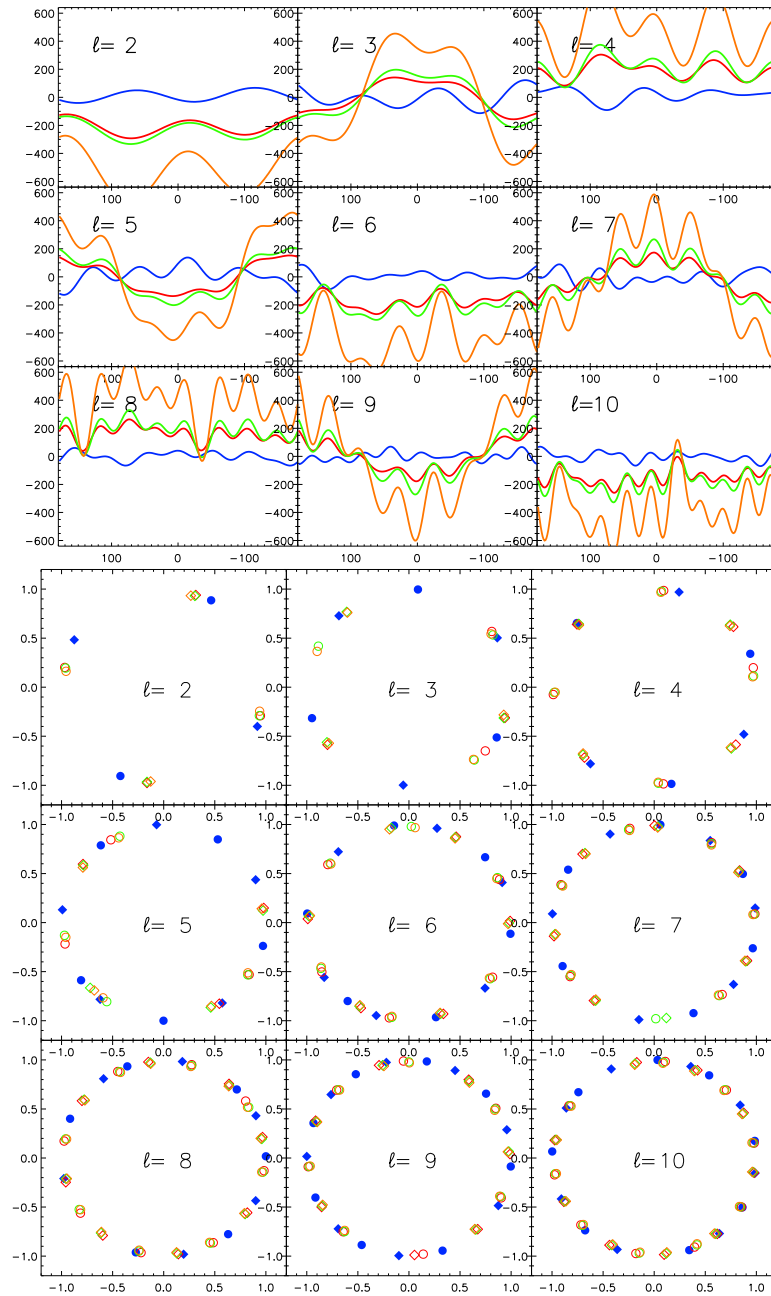


**Figure 3.** Top mosaic: the 1DFR curves for DILC (blue curves) and those of the foreground (sum of the synchrotron, free-free and dust templates) maps at Q channel (orange curves), V channel (green curves) and W channel (red curves). The  $x$  axis is  $\varphi$  and is plotted reversely to follow the conventional Galactic longitude coordinate  $l$  and the  $y$  axis is in unit of thermodynamic temperature ( $\mu\text{K}$ ). Notice strong anti cross correlation for the quadrupole. Bottom mosaic: the position of the local extrema plotted on unit circles. The angle between each point and the positive  $x$  axis is the position  $\varphi$  for each extrema of the 1DFR curves from the DILC map (blue filled sign) and those from foreground map at Q channel (orange open sign), V (green open sign) and W channel (red open sign). The circle and diamond signs represent peaks (local maxima) and troughs (local minima), respectively. The signs subtend about  $5^\circ$  so that, for example, one can see for  $l = 10$  there are 12 out of totally 16 local extrema of DILC 1DFR curves located within  $5^\circ$  of those of W channel foreground curve.

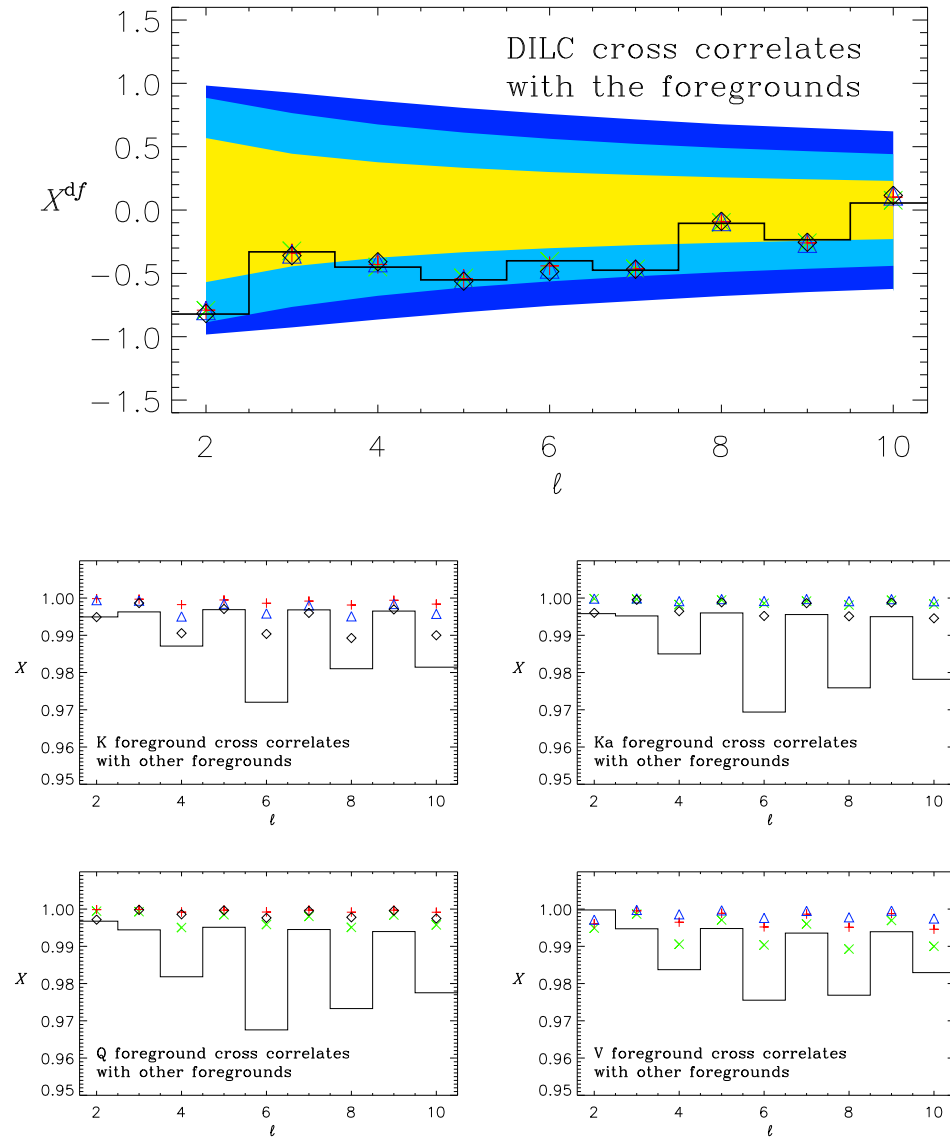


**Figure 4.** Cross correlation of the 1DFR curves from the DILC map with those from WMAP foreground maps (top panel) at K channel (green  $\times$ ), Ka channel (red  $+$  signs), Q (blue  $\triangle$  signs), V (black  $\diamond$ ), W (black line) and cross correlation of the 1DFR curves between the foregrounds (bottom 4 panels). Note that 8 out of 9 modes are negatively correlated, the probability for which to happen is  $C_1^9(2)^{-9} \simeq 0.0176$ . The yellow, light blue and dark blue areas denote 1, 2 and 3  $\sigma$  respectively (68.27%, 95.45% and 99.73%) of  $10^5$  Monte Carlo simulations.

positive and negative  $X$  should be equally  $1/2$ . One can see that eight out of the nine modes (except  $\ell = 10$ )  $X < 0$ , an outcome for which the probability is  $C_1^9(2)^{-9} \simeq 0.0176$ .

Secondly, the cross correlation in quadrupole is below  $-0.8$  (at around 90% CL). In our previous publication [11], we use cross correlation of phases between the DILC and foreground maps to examine foreground contamination. The most prominent correlation appears in octupole, which renders the significance level as low as 0.06. Although we do not claim that the quadrupole-octupole alignment is directly caused by the foregrounds, we can at least claim that since there is significant foreground contamination, such alignment is not cosmological. In the lower 4 panels of Figure 4 we also show the cross correlation between the foregrounds, which are all above 0.96.

#### *4.2. Correlation of extrema of the 1DFR curves*

In our previous publication [11], we used a 1DFR on the 9 modes  $2 \leq \ell \leq 10$  of the DILC map and examined the positions of the global extrema of the 9 curves. If the signal were Gaussian, the global extrema should distribute randomly on the  $\varphi$  axis. We found that the extrema are concentrated around  $\varphi = 180^\circ$  and avoid the  $\varphi = 0$  (Galactic centre) with significance level below 0.5%, which is a strong indication that the global extrema of the DILC map are non-randomly distributed due to some influence related to a Galactic-coordinate frame. Here we further examine the local extrema of the 1DFR curves of the DILC map and their correlation with those of the foregrounds.

In order to extract information about correlation of extrema between DILC and the foregrounds, we use the following method: for each foreground extremum, we search for its nearest DILC extremum and denote their distance by  $|\Delta\varphi_\ell(i)|$ , where  $i$  denotes the  $i$ th extremum of the foreground curve. The collection of the separation angles for each  $\ell$  is to be compared with the distribution of  $10^5$  Monte Carlo simulation on the GRF extrema against the foreground ones. In the top mosaic of Figure 5 we show the cumulative probability distribution of the separation angles between the DILC and W channel foreground extrema (red curves) and that of separation angles of  $10^5$  realizations of simulated GRF and W channel foreground extrema (black). The bottom panel is the significance level from Kolmogorov-Smirnov (K-S) test for the distribution of extrema of DILC with foreground maps at K channel (green  $\times$  signs), Ka channel (red  $+$  signs), Q (blue  $\triangle$  signs), V (black  $\diamond$  signs), W (black line). One can see that for  $\ell = 2$  and 6, the significance levels are all below 0.1 for all channels, and specifically, the significance levels are below 0.03 for the V channel, which is also the channel with the highest weight assigned by WMAP in the internal linear combination of multi-frequency cleaning to extract the CMB signal.

#### *4.3. Cross correlation with foreground templates independent from WMAP data*

To further certify foreground contamination in the DILC map, we also test various other full-sky foreground templates that are measured, collected or derived independently from the WMAP data. The existing foreground templates are the 408 MHz radio continuum

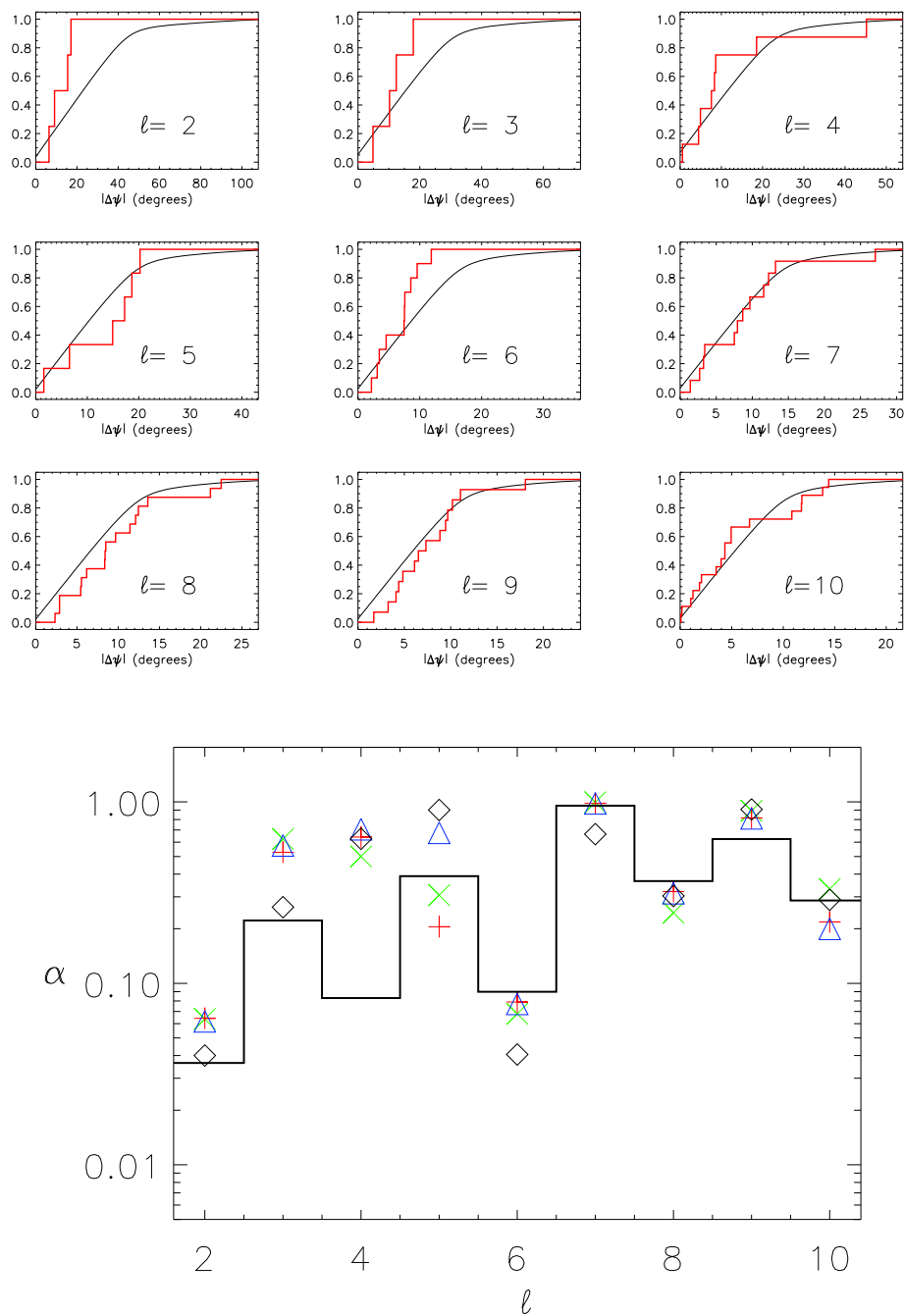


**Figure 5.** Top mosaic: the cumulative probability distribution of the separation angles (the angle of the nearest extremum) between the DILC and the W channel foreground extrema is plotted in red curves and the cumulative probability distribution of the separation angles from  $10^5$  Monte Carlo simulation is in black. The bottom panel is the significance level from K-S test for the distribution of extrema of DILC with foreground maps at K channel (green  $\times$  signs), Ka channel (red  $+$  signs), Q (blue  $\triangle$  signs), V (black  $\diamond$  signs), W (black line). For  $\ell = 2$  and  $6$ , the significance levels are below 0.04 for the V channel, which is also the most weighted channel by WMAP in internal linear combination of multi-frequency cleaning to extract the CMB signal.

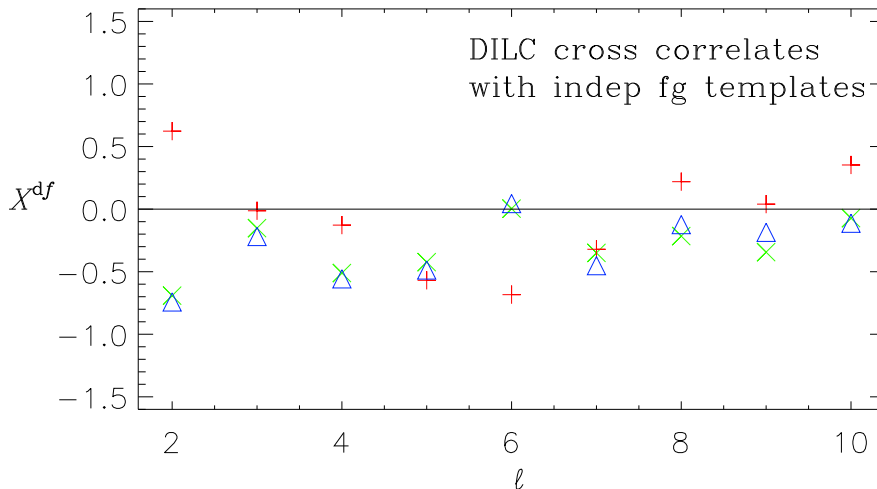


**Figure 6.** Cross correlation of the 1DFR curves from the DILC map with those from full-sky foreground templates that are observed, collected or derived independently from the WMAP data. These independent templates are the 408 MHz Continuum Survey (green  $\times$ ) for synchrotron emission,  $H\alpha$  map for free-free emission (red  $+$  signs), and the dust template extrapolated from COBE/DIRBE data (blue  $\Delta$  signs). For the synchrotron and dust templates, 8 of the 9 modes are negatively correlated with the DILC, the probability is  $C_1^9(2)^{-9} \simeq 0.0176$ .

survey [36] tracing the synchrotron pattern, the  $H\alpha$  template for thermal bremsstrahlung (free-free emission) [30], and the dust template extrapolated from COBE/DIRBE data to microwave frequencies [31]. We repeat the cross correlation of the 1DFR curves in Section 4.1 and show the cross correlation coefficient  $X$  in Fig.6. For both the synchrotron and dust templates, 8 of the 9 modes are negatively correlated with the DILC, the probability of this happening in the absence of real correlation only being  $C_1^9(2)^{-9} \simeq 0.0176$ . We find no significant evidence of cross-correlation with the  $H\alpha$  template, but this is not unexpected since this makes only a small contribution to the expected foreground at relevant frequencies. One should note that, although the 408 MHz map and the dust template are templates relating to single foreground components, they can be considered as total foreground templates as they represent the dominant component at the corresponding frequencies. Their correlation with the DILC strengthens the claims we made in the previous section.

## 5. Cross correlations with the foregrounds as an estimate on the foreground contamination

### 5.1. Minimum variance optimization and foreground residuals

In the last section, we have shown through strong cross correlation and peak correlation that the DILC signal is probably contaminated with foregrounds. We now examine the

concept of multi-frequency cleaning method and how foreground residuals propagate into the final map. Multi-frequency cleaning has been the workhorse for retrieving the CMB signal from polluted data. It is based on the concept that the CMB signal exists, among different frequency maps, as a frequency independent component [5, 38] (see also [26]):

$$T^i = T^{\text{cmb}} + F^i, \quad (5.1)$$

where  $T^i$  represents the total measured signal at frequency band  $i$ ,  $T^{\text{cmb}}$  the frequency independent (i.e. the CMB) signal, and  $F^i$  the foreground at frequency band  $i$  (here we assume noise is not important). This frequency-independent component can be flushed out with an internal linear combination on  $M$  frequency bands of maps with weighting coefficients  $\sum_{i=1}^M w_i = 1$ :

$$T^{\text{ilc}} = \sum_{i=1}^M w_i T^i = T^{\text{cmb}} + \sum_{i=1}^M w_i F^i, \quad (5.2)$$

where  $T^{\text{ilc}}$  represents the ILC map. The *a priori* assumption that the frequency independent component should be statistically independent with others ensures the variance of the ILC map is the sum of the variances of the two parts:

$$\text{var}[T^{\text{ilc}}] = \text{var}[T^{\text{cmb}}] + \text{var}\left[\sum_{i=1}^M w_i F^i\right]. \quad (5.3)$$

Therefore if one is to minimize the variance of the ILC map by  $\partial \text{var}[T^{\text{ilc}}]/\partial w_i = 0$ , it is equivalent to minimizing the variance of linear combination of the foregrounds,

$$\frac{\partial \text{var}[T^{\text{ilc}}]}{\partial w_i} \equiv \frac{\partial \text{var}\left[\sum_{i=1}^M w_i F^i\right]}{\partial w_i}, \quad (5.4)$$

thus reducing most the residuals to produce a map closest to the CMB. The WMAP DILC map is thus produced by employing the minimum variance optimization in the pixel domain in 12 separate regions, where Region 0 marks the largest region for  $|b| \geq 15^\circ$ , and Region 1 – 11 for those around the Galactic plane. In each region the 5 frequency maps are linearly combined and a set of weighting coefficients  $w_i^{(R)}$  are obtained in such a way that the resultant variance is minimum.

It is worth noting that Equation (5.3) requires statistical independence that is defined between the foregrounds and an ensemble of universes, but the fact that we have only one universe shall introduce some error in the minimization process. Furthermore, since the minimum variance optimization takes on the *overall* variance of the map, instead of the individual multipoles as the method by [59, 60, 18], there is no guarantee that the contamination from the foregrounds in each multipole  $\ell$  will be minimum (let alone zero). A spherical harmonic decomposition of Equation (5.2) gives

$$a_{\ell m}^{\text{dilc}} = a_{\ell m}^{\text{cmb}} + \sum_i w_i f_{\ell m}^i, \quad (5.5)$$

where  $f_{\ell m}^i$  represents the spherical harmonic coefficients for the foreground map  $F^i$ . For higher multipoles, the power spectrum  $C_\ell$  of the DILC should be close to that of CMB as there are more  $m$  modes participating in the summation  $(2\ell + 1)^{-1} \sum_m |a_{\ell m}^{\text{dilc}}|^2$ , as long

as the foreground residual  $\sum w_i f_{\ell m}^i$  is more or less non-correlated between each  $m$  of the same  $\ell$  (like white noise). On the other hand, for lower multipoles, the discrepancy between CMB and the DILC can be prominent when the foreground residuals are correlated.

From the significant cross and extremum correlation as shown in Figure 4 and Figure 5, it is indeed likely that the foreground residual is still a non-negligible part for low multipoles in the DILC map, unless the true CMB signal happens to 'resemble' the foregrounds, an eventuality which has a small probability.

### 5.2. Estimate of the foreground contamination

To make an estimate of the foreground contamination present in the DILC map, we can first of all write

$$f_{\ell m}^i = \sigma_{\ell}^{f^i} f_{\ell m}, \quad (5.6)$$

where  $\sigma_{\ell}^{f^i}$  is the r.m.s. of the fluctuation of  $f_{\ell m}^i$  and  $f_{\ell m}$  is the *unitary* foreground signal (related to morphology) with its r.m.s. of fluctuation  $\sigma_{\ell}^f = 1$ . Such a degeneracy can be seen in Figure 4 that most cross-correlations between foregrounds are above 0.99 (except with the W channel  $\sim 0.97$ ).

We now calculate the cross correlation coefficient of the 1DFR curves between the true CMB and the unitary foreground signal:

$$\begin{aligned} X_{\ell}^{cf} &= \frac{1}{2\pi} \int_0^{2\pi} \frac{\sum_{m \neq 0} a_{\ell m}^{\text{cmb}} \exp(im\varphi) \sum_{m' \neq 0} f_{\ell m'} \exp(im'\varphi)}{\sigma_{\ell}^{\text{cmb}} \sigma_{\ell}^f} d\varphi \\ &= \frac{2 \sum_{m=1}^{\ell} |a_{\ell m}^{\text{cmb}}| |f_{\ell m}| \cos(\Phi_{\ell m}^{\text{cmb}} - \Phi_{\ell m}^f)}{\sigma_{\ell}^{\text{cmb}}}. \end{aligned} \quad (5.7)$$

Although the CMB and the foregrounds should be statistically independent, i.e.  $\langle X_{\ell}^{cf} \rangle = 0$ , the fact that we only have one realization of the CMB fluctuation makes this parameter crucial, especially for low multipoles.

To relate the  $X_{\ell}^{cf}$  to the measured  $X_{\ell}^{\text{df}^i}$ , we first show, in the top panel of Figure 7, the cross-correlation of the foreground residuals with the foregrounds. The DILC map is processed with 12 sets of weighting coefficients  $w_i^{(R)}$ , where  $i = 1 - 5$  represent K, Ka, Q, V and W bands, respectively and  $(R)$  indicates Regions 0 – 11, so for the foreground residual we use a linear combination of the WMAP foregrounds on 12 separated regions to obtain the whole sky map:

$$R(\theta, \varphi) = \sum_{R=0}^{11} \sum_{i=1}^5 w_i^{(R)} F_{(R)}^i, \quad (5.8)$$

from which we produce the 1DFR curves  $R_{\ell}$ . One can see that for  $\ell = 2, 3$  and 4, the foreground residual has significant anti-correlation with the foregrounds. We caution that the WMAP foregrounds are retrieved via the Maximum Entropy Method, not by direct subtraction of the DILC signal off the frequency maps, so the DILC is not a simple sum of the true CMB and the foreground residual as Equation (5.3). For the

modes in which the residual has significant correlation, we express the residuals in terms of the unitary foreground signals  $\epsilon_\ell f_{\ell m}$ :

$$a_{\ell m}^{\text{dilc}} \simeq a_{\ell m}^{\text{cmb}} + \epsilon_\ell f_{\ell m}, \quad (5.9)$$

where  $\epsilon_\ell$  is the contamination parameter at multipole number  $\ell$ . For other multipoles, this approach means we are estimating the most possible contamination.

The cross correlation between the 1DFR curves of the DILC and the foreground maps can be written as

$$\begin{aligned} X_\ell^{\text{df}^i} &= \frac{1}{2\pi} \int_0^{2\pi} \frac{\sum_{m \neq 0} a_{\ell m}^{\text{dilc}} \exp(im\varphi) \sum_{m' \neq 0} f_{\ell m'}^i \exp(im'\varphi)}{\sigma_\ell^{\text{dilc}} \sigma_\ell^{\text{f}^i}} d\varphi \\ &= \frac{\epsilon_\ell + 2 \sum_{m=1}^\ell |a_{\ell m}^{\text{cmb}}| |f_{\ell m}| \cos(\Phi_{\ell m}^{\text{cmb}} - \Phi_{\ell m}^{\text{f}})}{\sqrt{\epsilon_\ell^2 + (\sigma_\ell^{\text{cmb}})^2 + 4\epsilon_\ell \sum_{m=1}^\ell |a_{\ell m}^{\text{cmb}}| |f_{\ell m}| \cos(\Phi_{\ell m}^{\text{cmb}} - \Phi_{\ell m}^{\text{f}})}}. \end{aligned} \quad (5.10)$$

We can now denote  $X_\ell^{\text{df}^i} \equiv X_\ell^{\text{df}}$  as it is independent of the individual foreground channels. The measured  $X_\ell^{\text{df}^i}$ , as shown in the top panel of Figure 4, are indeed degenerate due to the resemblance in morphology between the foregrounds. With Equation (5.7) we can solve Equation (5.10) for  $\epsilon_\ell$ :

$$\epsilon_\ell = \sigma_\ell^{\text{cmb}} \left( -X_\ell^{\text{cf}} + X_\ell^{\text{df}} \sqrt{\frac{1 - (X_\ell^{\text{cf}})^2}{1 - (X_\ell^{\text{df}})^2}} \right). \quad (5.11)$$

Equation (5.11) describes the contamination parameter in relation to  $X_\ell^{\text{cf}}$  and  $X_\ell^{\text{df}}$ . In the middle panel of Figure 7 we plot the foreground contamination parameter  $\epsilon_\ell$  in unit of  $\sigma_\ell^{\text{cmb}}$  against the cross correlation coefficients  $X_\ell^{\text{df}}$ . The thick line is for zero correlation between CMB and the foregrounds:  $X_\ell^{\text{cf}} = 0$ , which is the case for high  $\ell$  with more  $m$  modes in the summation of Equation (5.7). For low  $\ell$ , however, the  $X_\ell^{\text{cf}}$  plays a major role. In the bottom panel of Figure 7 we use the mean value of the  $X_\ell^{\text{df}^i}$  from DILC and WMAP foreground maps in Figure 4 as input, and run  $10^6$  Monte Carlo simulations for the  $X_\ell^{\text{cf}}$ . The foreground contamination is illustrated by the ratio  $\epsilon_\ell/\sigma_\ell^{\text{cmb}}$  at the values of 1, 2 and 3  $\sigma$  thresholds (yellow, light blue and dark blue areas, respectively). Note that the foreground contamination shown in this way is independent of the underlying CMB power spectrum, and we assume the foreground residuals in the DILC map has the same morphology as the foregrounds themselves, so we are estimating an upper limit on the contamination ratio.

## 6. Conclusion and Discussion

In this paper we have proceeded from the basic assumption that the CMB should have no or little correlation (within cosmic variance limit) with the foregrounds, to examine foreground contamination in the WMAP DILC map. We use the newly-developed representation 1DFR of the spherical harmonic coefficients for cross and peak correlation. The 1DFR has an advantage in that the  $m = 0$  modes do not alter the

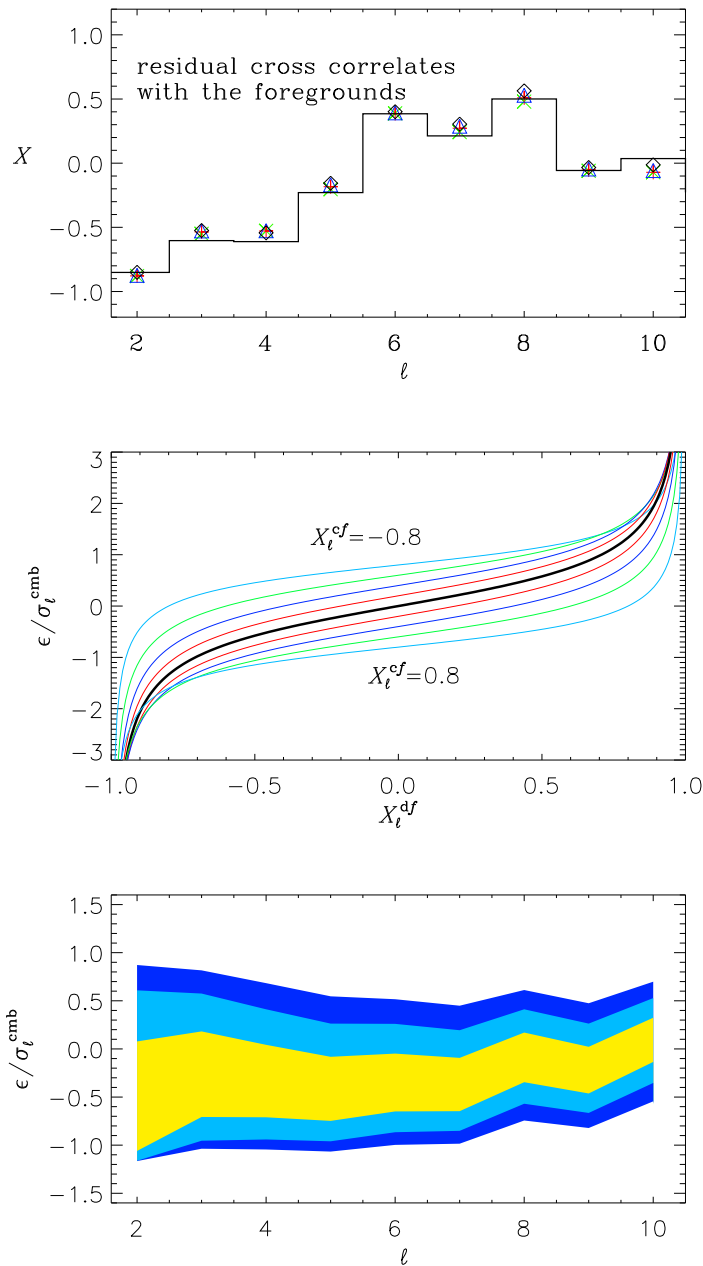


**Figure 7.** The top panel shows the cross-correlation between the foreground residuals  $R_\ell$  and the foregrounds  $F_\ell^i$  and the other two are the foreground contamination parameter  $\epsilon_\ell$  in units of  $\sigma_\ell^{\text{cmb}}$ . Middle panel is the contamination ratio  $\epsilon_\ell/\sigma_\ell^{\text{cmb}}$  against the cross correlation coefficients  $X_\ell^{\text{df}}$  for DILC and the foregrounds (from Equation (5.11)). The curves are for  $X_\ell^{\text{cf}} = -0.8$  (the top) downwards with increment 0.2 to  $X_\ell^{\text{cf}} = 0.8$ . The thick line is for zero correlation:  $X_\ell^{\text{cf}} = 0$  between CMB and the foregrounds. In the bottom panel, we take the mean value of  $X_\ell^{\text{df}^i}$  from top panel of Figure 4 as input and perform  $10^6$  Monte Carlo simulations for the CMB and the  $X_\ell^{\text{cf}}$ . The yellow, light blue and dark blue areas illustrate the contamination ratio  $\epsilon_\ell/\sigma_\ell^{\text{cmb}}$  at 1, 2 and 3  $\sigma$  thresholds, respectively.

morphology, and when using the standard definition of cross correlation of the 1D curves, they are intrinsically excluded in the calculation.

We have tested the DILC map for  $2 \leq \ell \leq 10$ , although any diagnostics of correlation can be applied to all  $\ell$  modes for both the *WMAP* and the upcoming *Planck* data. We find that eight out of nine modes are negatively-correlated, for which the probability is only 0.0176 if they are really independent. We also find the local extrema of the 1DFR curves are correlated, particularly for  $\ell = 2$  and 6 modes, with significance level less than 0.04. Both analyses have indicated that the DILC quadrupole is contaminated with foregrounds (with cross correlation coefficient  $X < -0.8$  and extremum statistics at significance level  $\alpha < 0.04$ ). We then used the cross correlation coefficients to explore the level of the foreground contamination.

The axiom that the CMB has no correlation with the foregrounds provides the most fundamental criterion that should be applied as a foreground cleaning check before any Gaussianity tests are performed and cosmologists get carried away by suggestions of new physics. We suggest that for the upcoming *Planck* mission, one should not ignore the kind of information we have presented here, before any scientific conclusion is reached.

One final remark for our results is that the DILC map is derived from the concept of minimum variance optimization under the *a priori* assumption that CMB and the foregrounds are statistically independent. That we have only one universe, hence there is inevitably accidental correlation shall introduce some error in the estimation of the weighting coefficients, and consequently introduce residuals in the resultant map. Even if the correlation between the CMB and the foregrounds happens to be zero, the variance of the foreground residuals is minimum, but not necessarily zero. Although we can extract the angular power spectrum as close as possible to that of the CMB using such methods, the signal obtained in general still contains residuals.

## Acknowledgments

PC would like to thank the Niels Bohr International Academy for their support during the Summer Institute when this paper was written. We acknowledge the use of the NASA Legacy Archive for extracting the *WMAP* data. We also acknowledge the use of HEALPIX ‡ package [34] to produce  $a_{\ell m}$  from the *WMAP* data and the use of GLESP § package [23].

## References

- [1] L R Abramo Bernui A Ferreira I. S Villela T and Wuensche C A, *Alignment tests for low CMB multipoles*, 2006 *Phys. Rev. D* submitted [astro-ph/0604346]
- [2] L R Abramo L Sodre Jr and Wuensche C A, *Anomalies in the low CMB multipoles and extended foregrounds*, 2006 *Phys. Rev. D* submitted [astro-ph/0605269]

‡ <http://www.eso.org/science/healpix/>

§ <http://www.glesp.nbi.dk>

- [3] Bardeen J M Bond J R Kaiser N and Szalay A S, *The statistics of Peaks of Gaussian Random Fields*, 1986 *Astrophys. J* **304** 15 []
- [4] Bennett C L *et al* *First-Year Wilkinson Microwave Anisotropy Probe (WMAP) Observations: Preliminary Maps and Basic Results*, 2003 *Astrophys. J. Supp.* **148** 1 [astro-ph/0302207]
- [5] Bennett C L *et al* *First-Year Wilkinson Microwave Anisotropy Probe (WMAP) Observations: Foreground Emission*, 2003 *Astrophys. J. Supp.* **148** 97 [astro-ph/0302208]
- [6] Bernui A Mota B Reboucas M J and Tavakol R, *Mapping the large-scale anisotropy in the WMAP data*, 2006 *Phys. Rev. D* submitted [astro-ph/0511666]
- [7] Bond J R and Efstathiou G, *The statistics of cosmic background radiation fluctuations*, 1987 *Mon. Not. R. Astron. Soc.* **226** 655 []
- [8] C Burigana A Gruppuso and F Finelli, *On the dipole straylight contamination in spinning space missions dedicated to CMB anisotropy*, 2006 *Mon. Not. R. Astron. Soc.* accepted [astro-ph/0607506]
- [9] Cabella P Hansen F Marinucci D Pagano D and Vittorio N, *Search for non-Gaussianity in pixel, harmonic and wavelet space: compared and combined*, 2004 *Phys. Rev. D* **69** 063007 [astro-ph/0401307]
- [10] Chiang L-Y, *The Importance of Fourier Phases for the Morphology of Gravitational Clustering*, 2001 *Mon. Not. R. Astron. Soc.* **325** 405 [astro-ph/0011021]
- [11] Chiang L-Y Naselsky P D and Coles P, *Testing the Gaussian Random Hypothesis with the Cosmic Microwave Background Temperature Anisotropies in the 3-Year WMAP Data*, 2006 *Astrophys. J* submitted [astro-ph/0603662]
- [12] Chiang L-Y Naselsky P D Verkhodanov O V and Way M J, *Non-Gaussianity of the derived maps from the first-year WMAP data*, 2003 *Astrophys. J* **590** L65 [astro-ph/0303643]
- [13] Chiang L-Y and Naselsky P D, *Auto and cross correlation of phases of the whole-sky CMB and foreground maps from the 1-year WMAP data*, 2006 *Int. J. Mod. Phys. D* in press [astro-ph/0407395]
- [14] Coles P Dineen P Earl J and Wright D, *Phase Correlations in Cosmic Microwave Background Temperature Maps*, 2004 *Mon. Not. R. Astron. Soc.* **350** 989 [astro-ph/0310252]
- [15] Copi C J Huterer D and Starkman G D, *Multipole Vectors—a new representation of the CMB sky and evidence for statistical anisotropy or non-Gaussianity at  $2 \leq \ell \leq 8$* , 2004 *Phys. Rev. D* **70** 043515 [astro-ph/0310511]
- [16] Copi C J Huterer D Schwarz D J and Starkman G D, *The Uncorrelated Universe: Statistical Anisotropy and the Vanishing Angular Correlation Function in WMAP Years 1-3*, *Phys. Rev. D* submitted [astro-ph/0605135]
- [17] Cruz M Cayon L Martinez-Gonzalez E Vielva P and Jin J, *The non-Gaussian Cold Spot in the 3-year WMAP data*, *Astrophys. J* submitted [astro-ph/0603859]
- [18] de Oliveira-Costa A and Tegmark M, *CMB multipole measurements in the presence of foregrounds*, 2006 *Phys. Rev. D* submitted [astro-ph/0603369]
- [19] de Oliveira-Costa A Tegmark M Zaldarriaga M and Hamilton A, *The significance of the largest scale CMB fluctuations in WMAP*, 2004 *Phys. Rev. D* **69** 063516 [astro-ph/0307282]
- [20] Dineen P and Coles P, *Faraday Rotation as a Diagnostic of Galactic Foreground Contamination of CMB Maps*, 2003 *Mon. Not. R. Astron. Soc.* **347** 52 [astro-ph/0306529]
- [21] Dineen P and Coles P, *A Faraday Rotation Template for the Galactic Sky*, 2005 *Mon. Not. R. Astron. Soc.* **362** 403 [astro-ph/0410636]
- [22] Dineen P and Coles P, *Multivariate Non-Normality in the WMAP 1st Year Data*, 2006 *Mon. Not. R. Astron. Soc.* submitted [astro-ph/0511802]
- [23] Doroshkevich A G *et al* *Gauss-Legendre Sky Pixelization (GLESP) for CMB maps*, 2003 *Int. J. Mod. Phys. D* **14** 275 [astro-ph/0305537]
- [24] Efstathiou G, *The Statistical Significance of the Low CMB Multipoles*, 2003 *Mon. Not. R. Astron. Soc.* **346** L26 [astro-ph/0306431]
- [25] Efstathiou G, *A Maximum Likelihood Analysis of the Low CMB Multipoles from WMAP*, 2004

- Mon. Not. R. Astron. Soc.* **348** 885 [astro-ph/0310207]
- [26] Eriksen H K Banday A J Górski K M and Lilje P B, *On Foreground Removal from the Wilkinson Microwave Anisotropy Probe Data by an Internal Linear Combination Method: Limitations and Implications*, 2004 *Astrophys. J* **612** 633 [astro-ph/0403098]
- [27] Eriksen H K Hansen F K Banday A J Gorski K M and Lilje P B, *Asymmetries in the CMB anisotropy field*, 2004 *Astrophys. J* **605** 14 [astro-ph/0307507]
- [28] Eriksen H K Novikov D I Lilje P B Banday A J and Górski K M, *Testing for non-Gaussianity in the WMAP data: Minkowski functionals and the length of the skeleton*, 2004 *Astrophys. J* **612** 64 [astro-ph/0401276]
- [29] Ferreira P Magueijo J and Górski K M, *Evidence for non-Gaussianity in the COBE DMR Four Year Sky Maps*, 1998 *Astrophys. J* **503** L1 [astro-ph/9803256]
- [30] Finkbeiner D, *A Full-Sky H-alpha Template for Microwave Foreground Prediction*, 2003 *Astrophys. J. Supp.* **146** 407 [astro-ph/0301558]
- [31] Finkbeiner D Davis M and Schlegel D J, *Extrapolation of Galactic Dust Emission at 100 Microns to CMBR Frequencies Using FIRAS*, 1999 *Astrophys. J* **524** 867 [astro-ph/9905128]
- [32] Gaztanagz E and Wagg J, *3-point temperature anisotropies in WMAP: Limits on CMB non-Gaussianities and non-linearities*, 2003 *Phys. Rev. D* **68** 021302 [astro-ph/0305327]
- [33] Gordon C Hu W Huterer D Crawford T *Spontaneous Isotropy Breaking: A Mechanism for CMB Multipole Alignments*, 2005 *Phys. Rev. D* **72** 103002 [astro-ph/0509301]
- [34] Górski K M Hivon E and Wandelt B D, 1999 *Proc. of the MPA/ESO Cosmology Conference "Evolution of Large-Scale Structure"* (PrintPartners Ipskamp, NL) [astro-ph/9812350]
- [35] Hansen F K Cabella P Marinucci D and Vittorio N, *Asymmetries in the local curvature of the WMAP data*, 2004 *Astrophys. J. Lett.* **607** 67 [astro-ph/0402396]
- [36] Haslam C G T Salter C J Stoffel H and Wilson W E, *A 408 MHz All-Sky Continuum Survey. II The Atlas of Contour Maps*, 1982 *Astro. & Astrophys.* **47** 1 []
- [37] Hinshaw G *et al* *First-Year Wilkinson Microwave Anisotropy Probe (WMAP) Observations: The Angular Power Spectrum*, 2003 *Astrophys. J. Supp.* **148** 135 [astro-ph/0302217]
- [38] Hinshaw G *et al* *Three-Year Wilkinson Microwave Anisotropy Probe (WMAP) Observations: Temperature Analysis*, 2006 *Astrophys. J* submitted [astro-ph/0603451]
- [39] Inoue K T and Silk J, *Local Voids as the Origin of Large-angle Cosmic Microwave Background Anomalies*, 2006 *Astrophys. J* [astro-ph/0602478]
- [40] Jaffe T *et al* *Evidence of vorticity and shear at large angular scales in the WMAP data: a violation of cosmological isotropy?*, 2005 *Astrophys. J. Lett.* **629** 1 [astro-ph/0503213]
- [41] Komatsu E *et al* *First-Year Wilkinson Microwave Anisotropy Probe (WMAP) Observations: Tests of Gaussianity*, 2003 *Astrophys. J. Supp.* **148** 119 [astro-ph/0203223]
- [42] Land K and Magueijo J, *The axis of evil*, 2005 *Phys. Rev. Lett.* **95** 071301 [astro-ph/0502237]
- [43] Larson D L and Wandelt B D, *The Hot and Cold Spots in the WMAP Data are Not Hot and Cold Enough*, 2004 *Astrophys. J. Lett.* **613** 85 [astro-ph/0404037]
- [44] Matsubara T *Phase Correlations in Non-Gaussian Fields*, 2003 *Astrophys. J. Lett.* **591** 79 [astro-ph/0303278]
- [45] McEwen J D Hobson M P Lasenby A N and Mortlock D J, *A high-significance detection of non-Gaussianity in the WMAP 1-year data using directional spherical wavelets*, 2005 *Mon. Not. R. Astron. Soc.* **359** 1583 [astro-ph/0406604]
- [46] McEwen J D Hobson M P Lasenby A N and Mortlock D J, *A high-significance detection of non-Gaussianity in the WMAP 3-year data using directional spherical wavelets*, *Mon. Not. R. Astron. Soc.* submitted [astro-ph/0604305]
- [47] Mukherjee P and Wang Y, *Wavelets and WMAP non-Gaussianity*, 2004 *Astrophys. J* **613** 51 [astro-ph/0402602]
- [48] Naselsky P D Chiang L-Y Verkhodanov O V and Novikov I D, *Foreground analysis from the 1-year WMAP data*, 2005 *Int. J. Mod. Phys. D* **14** 1273 [astro-ph/0405523]
- [49] Naselsky P D Chiang L-Y Olesen P and Novikov I D, *Statistics of phase correlations as a test for*

- non-Gaussianity of the CMB maps*, 2005 *Phys. Rev. D* **72** 3512 [astro-ph/0505011]
- [50] Naselsky P D Doroshkevich A and Verkhodanov O V, *Phase cross-correlation of the WMAP ILC map and foregrounds*, 2003 *Astrophys. J. Lett.* **599** 53 [astro-ph/0310542]
- [51] Naselsky P D Doroshkevich A and Verkhodanov O V, *Cross-correlation of the CMB and foregrounds phases derived from the WMAP data*, 2004 *Mon. Not. R. Astron. Soc.* 349 [astro-ph/0310601]
- [52] Naselsky P. D Novikov I D and Chiang L-Y, *Correlations from Galactic foregrounds in the 1-year Wilkinson Microwave Anisotropy Probe (WMAP) data*, 2006 *Astrophys. J* **642** 617 [astro-ph/0506466]
- [53] Park C-G, *Non-Gaussian Signatures in the Temperature Fluctuation Observed by the Wilkinson Microwave Anisotropy Probe*, 2004 *Mon. Not. R. Astron. Soc.* **349** 313 [astro-ph/0307469]
- [54] Park C-G, Park C and Gott J R III, *Cleaned Three-Year WMAP CMB Map: Magnitude of the Quadrupole and Alignment of Large Scale Modes*, 2006 *Astrophys. J* submitted [astro-ph/0608129]
- [55] Schwarz D J Starkman G D Huterer D and Copi C J, *Is the low- $l$  microwave background cosmic?*, 2004 *Phys. Rev. Lett.* **93** 221301 [astro-ph/0403353]
- [56] Smoot G F *et al* *Structure in the COBE differential microwave radiometer first-year maps*, L1 *Astrophys. J* **1992** 396 []
- [57] Spergel D N *et al* *Wilkinson Microwave Anisotropy Probe (WMAP) Three Year Results: Implications for Cosmology*, 2006 *Astrophys. J* submitted [astro-ph/0603449]
- [58] Spergel D N *et al* *First Year Wilkinson Microwave Anisotropy Probe (WMAP) Observations: Determination of Cosmological Parameters*, 2003 *Astrophys. J. Supp.* **148** 175 [astro-ph/0302209]
- [59] Tegmark M and Efstathiou G, *A method for subtracting foregrounds from multi-frequency CMB sky maps*, 1996 *Mon. Not. R. Astron. Soc.* **281** 1297 [astro-ph/9507009]
- [60] Tegmark M de Oliveira-Costa A and Hamilton A, *A high resolution foreground cleaned CMB map from WMAP*, 2003 *Phys. Rev. D* **68** 123523 [astro-ph/03022496]
- [61] Tojeiro R Castro P G Heavens A F and Gupta S, *Non-Gaussianity in the WMAP data using the peak-peak correlation function*, 2006 *Mon. Not. R. Astron. Soc.* **365** 265 [astro-ph/0507096]
- [62] Vielva P Martinez-Gonzalez E Barreiro R B Sanz J L and Cayon L, *Detection of non-Gaussianity in the WMAP 1-year data using spherical wavelets*, 2004 *Astrophys. J* **609** 22 [astro-ph/0310273]
- [63] White M Krauss L M and Silk J, *Cosmic Variance in Cosmic Microwave Background Anisotropies: From 1 degrees to COBE*, 1993 *Astrophys. J* **418** 535 [astro-ph/9303009]